ACS OMEGA

Open Access

http://pubs.acs.org/journal/acsodf

Article

Evaluation of Structural, Magnetic, and Electromagnetic Properties of Co^{2+}-Substituted NiCuZn Ferrites

Babasaheb Ingale, Digambar Nadargi,* Jyoti Nadargi, Rangrao Suryawanshi, Hamid Shaikh, Mohammad Asif Alam, Mohaseen S. Tamboli, and Sharad S. Suryavanshi*

Cite This: *ACS Omega* 2023, 8, 30508−30518

Read Online

ACCESS | Metrics & More | Article Recommendations | Supporting Information

ABSTRACT: We report citrate gel-assisted autocombusted spinel-type Co^{2+}-substituted NiCuZn ferrites and their electromagnetic properties. Several complementary techniques were used to investigate the influence of Co on structural and electromagnetic properties of $Ni_{0.25-x}Co_xCu_{0.20}Zn_{0.55}Fe_2O_4$ with x = 0.00−0.25 (step of 0.05). XRD analysis confirmed the highly crystalline single-phase cubic spinel structure with a prominent peak of the (311) plane. FE-SEM analysis showed the loss of porous gel structure (colloidal backbone) due to addition of cobalt into the present ferrite system. The EDAX analysis confirmed the presence of Ni, Cu, Zn, Co, and O in accordance with the relative stoichiometry of Co-substituted NiCuZn ferrite. The electrical resistivity of ferrites is observed to decrease when Co^{2+} ions are substituted, regardless of AC and DC. The dielectric properties (ε' and ε'') of ferrites exhibited a consistent decrease as the frequency increased, and this trend persisted even at higher frequencies. VSM analysis showed the normal magnetic hysteresis of the developed ferrite system. At x = 0.05, the saturation magnetization of the ferrite was obtained to be the highest among the other substitution levels of Co. The Curie temperature fell down when there was a higher concentration of cobalt in the ferrite system (x = 0.20). After reaching a specific temperature, the μ_i values decreased abruptly, with an increase in the temperature. The steady state may be deduced from the fact that the constant real component of the initial permeability, μ', remained unchanged. However, with decreasing frequency, the values of μ'' decreased dramatically. The present NiCuZn ferrite series displays the enhanced dielectric properties suggesting the capability of potential candidates for microwave absorption applications with enhanced electromagnetic properties.

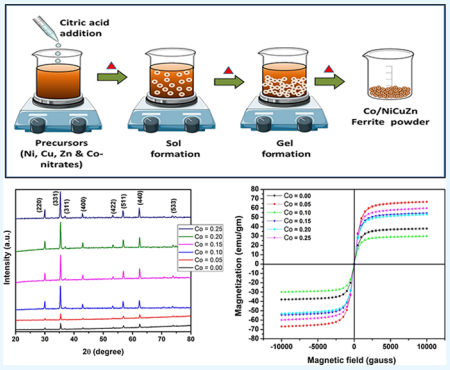

1. INTRODUCTION

From the family of spinel ferrites, NiCuZn has attracted researchers due to its fascinating properties such as high Curie temperature, saturation magnetization, and initial permeability and low ferromagnetic resonance (FMR) linewidth compared to the other ferrite materials. NiCuZn ferrites are promising candidates for several applications, including antibacterial agents,[1,2] recording heads,[3,4] microwave absorbers,[5,6] and high-frequency applications.[7,8] Because of the increasing need for miniaturization, versatile, and compact electronic gadgets, scientists are focusing their attention on high-power inductors. In order to achieve the goal of downsizing in energy storage devices, multilayer chip inductors (MLCIs) are widely used. Due to its high resistance and remarkable magnetic properties in high-frequency bands, NiCuZn ferrite has been extensively studied as a substrate magnetic material for MLCIs. Improved electromagnetic properties of nanoferrites are crucial for effective MLCIs to lower the ferrite volume. More study on NiCuZn ferrites has been done to explore the physical phenomena responsible for electromagnetic changes, which is necessary to obtain the technical benefits of miniaturizing dense cores for high frequencies.

In the literature, numerous studies have been conducted to investigate both the physicochemical properties and manufacturing technique of NiCuZn spinel ferrites. The substitution of metallic ions such as dysprosium (Dy), terbium (Tb), magnesium (Mg), manganese (Mn), copper (Cu), lithium (Li), and so on may alter the electromagnetic characteristics of NiCuZn spinel ferrites.[9−16] With this motivation, in the present work, a focus is made to study Co^{2+}-substituted NiCuZn ferrites for the improved electromagnetic properties. When compared to their bulk magnetic properties, Co^{2+}-substituted spinel ferrites have a distinct set of structural and electromagnetic features that set them apart. Co^{2+} is a rapidly relaxing ion that may improve the microwave characteristics of electronic devices such as switching devices and memory components. The Curie temperature of cobalt ferrite is very

Received: May 29, 2023
Accepted: July 31, 2023
Published: August 8, 2023

high (1150 °C), and therefore, thermal stability associated with the magnetic property becomes significant. It has also been noticed that cobalt ferrite has shown to be a good and acceptable choice for high-sensitivity magnetic sensors due to the fact that it has a substantial magnetomechanical effect.

Furthermore, owing to the fact that Co^{2+} ions have a positive K_1 value at the octahedral position, they have garnered a lot of interest. According to the findings of Mazen et al.,[7] the saturation magnetization (M_s) of nickel-copper ferrites rises with the increasing concentration of cobalt. This may be explained by the larger orbital contribution of Co^{2+} relative to the contribution of the other ions in the compound. It was also shown that the coercivity H_c of ferrites increased with the amount of cobalt present in the mineral.[8] Following the incorporation of cobalt, the core losses and magnetization mechanism of the NiCuZn ferrites have been investigated by Lucas et al.[17] According to the findings, the fluctuation in anisotropy that was generated by the Co^{2+} ions led to a significant reduction in the amount of core loss.

The impacts of substituting Co^{2+} ions in NiCuZn ferrites on structural, morphological, and electromagnetic properties are described herein.

2. EXPERIMENTAL PROCEDURE

2.1. Materials Used and Synthesis Route. In order to produce Co^{2+}-substituted NiCuZn ferrites, the overall method entails carrying out the following two significant steps: (i) the synthesis of material powder using sol−gel combustion followed by the creation of pellets and/or toroids and (ii) investigation/characterization of the developed ferrite material.

In a typical synthesis, AR-grade nitrates cobalt nitrate hexahydrate ($Co(NO_3)_2{\cdot}6H_2O$), nickel nitrate hexahydrate ($Ni(NO_3)_2{\cdot}6H_2O$), copper nitrate hexahydrate ($Cu(NO_3)_2{\cdot}6H_2O$), zinc nitrate tetrahydrate ($Zn(NO_3)_2{\cdot}4H_2O$), and ferric nitrate nonahydrate ($Fe(NO_3)_3{\cdot}9H_2O$) and citric acid ($C_6H_8O_7$) were obtained from Sigma Aldrich and were used as received. Stoichiometry of the redox mixture for combustion was estimated and held constant based on the total oxidizing and reducing valence of the oxidizer and the reductant (1:1 mol). In the appropriate quantity of distilled water, the precursors and reagent were thoroughly combined and homogenized, as per the molar concentrations given in the Supporting Information (Table S1). The temperature of the sol was brought up to ∼100 °C. At the predetermined temperature, the sol viscosity steadily grew with increasing time, as predicted by the natural behavior. The highly viscous sol eventually reached the threshold for percolation, which led to the formation of a gel that was subsequently enriched with water. After that, the gel was subjected to further heat treatment at an even greater temperature (∼150−200 °C). The thick gel continued to foam, and finally, as the water evaporated, the gel started to exhaust into a quick flameless autocombustion process with the evolution of a considerable amount of gaseous products; following this, it got autoignited. The schematic illustration of the development of Co-substituted NiCuZn ferrite is shown in Figures 1 and 2.

Finally, the resulting powder was calcined in air at a temperature of 650 °C for 2 h in order to remove any residues of unreacted leftovers while maintaining the pure ferrite material. After that, using a manual pressing machine with a pressure of 1.5 tons/cm^2 and PVA as the binder, the powder was formed into pellets with a diameter of 15 mm and a thickness of 2 mm, as well as toroids with an inner diameter of

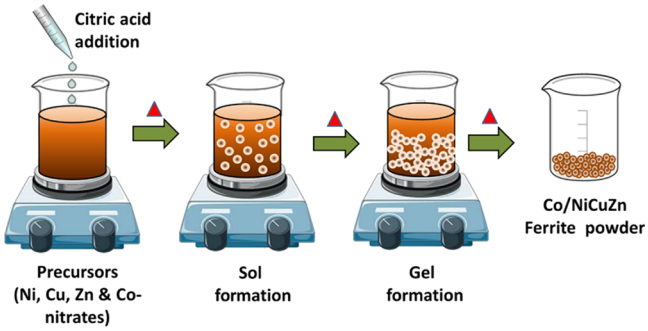

Figure 1. Schematic illustration for the development of Co-substituted NiCuZn ferrite gel by the use of a citrate-initiated sol−gel technique.

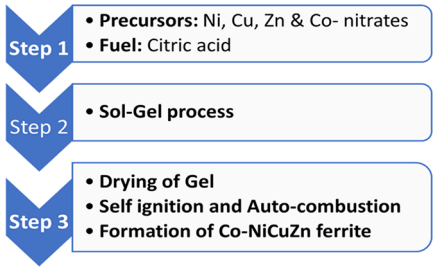

Figure 2. Schematic illustration of the complete process of Co-substituted NiCuZn ferrites.

1.5 cm, an outer diameter of 2.5 cm, and an average height of 0.3 cm. The pellets and the toroids were both sintered at a temperature of 950 °C for 4 h in air. The general composition of the developed ferrites is $Ni_{0.25-x}Co_xCu_{0.20}Zn_{0.55}Fe_2O_4$ with x = 0.00−0.25.

2.2. Characterization Techniques. The X-ray spectrographs were obtained using a Rigaku Ultima IV (Japan) X-ray powder diffraction instrument, which utilizes the Cu Kα (λ = 1.5406 Å) line. The suspension medium of xylene was utilized to determine the bulk densities using the liquid immersion technique. The analysis of morphology and particle size distribution was conducted using scanning electron microscopy (SEM) with a JEOL-JSM 6360 model. The chemical composition analysis of the developed ferrites was conducted using energy-dispersive X-ray (EDX) spectrographs. The hysteresis behavior of ferrites at a temperature of 80 K was recorded using a vibrating sample magnetometer (VSM) with the model 4500 EG and G, manufactured by Princeton Applied Research Corporation. The experimental setup involved the utilization of an LCR-Q meter, specifically the Hioki model 3532-50, to measure the initial permeability as a function of frequency and temperature. The two-probe method was employed to measure the DC resistivity within a temperature range of 300−773 K. The AC resistivity and dielectric parameters were determined by employing an LCR meter (model HP-4284A) at a temperature of 300 K, within the frequency range of 20 Hz to 1 MHz.

3. RESULTS AND DISCUSSION

3.1. Crystallographic Analysis (XRD). Figure 3 demonstrates the XRD pattern of developed Co-substituted NiCuZn ferrite samples with x = 0−0.25 for the general composition $Ni_{0.25-x}Co_xCu_{0.20}Zn_{0.55}Fe_2O_4$. All the samples possess a single-phase cubic spinel structure, and these structures match up

https://doi.org/10.1021/acsomega.3c03757
ACS Omega 2023, 8, 30508−30518

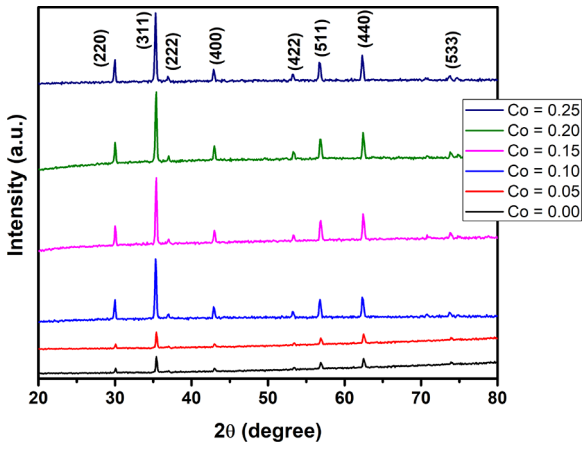

Figure 3. XRD spectra of the developed Co-substituted NiCuZn ferrites.

nicely with JCPDS card number 08-0234 to all the XRD patterns. The corresponding peaks were indicated as (220), (311), (222), (400), (422), (511), (440), and (533). For calculating the value of the lattice parameter (a), the most intense peaks were utilized. It is clearly seen that no impurity peaks are present in the developed ferrite samples. The ionic radius of Co^{2+} is 0.74 Å, which is somewhat greater than the ionic radius of Ni^{2+}, which is 0.72 Å. The expansion of the lattice results in an increase in the values of the lattice parameters. Numerous researchers have documented analogous increases in the lattice parameter as a function of dopant concentrations.[10]

This difference causes the lattice parameter (a) to rise, as seen in Table 1. Scherrer's formula was used to calculate the average crystallite size, denoted by the value D, of the ferrite nanoparticles based on the XRD peak broadening of the (331) plane.

$$D = \frac{K\lambda}{\beta \cos\theta} \tag{1}$$

where "λ" is the wavelength of X-ray radiation used, "β" is FWHM (in radians), "θ" is the angle of reflection, and "K" is the Scherrer constant. K in the Scherrer equation is not known for the present material system. K can have values anywhere from 0.62 and 2.08.

The Scherrer equation is widely acknowledged for its consideration of the relationship between the broadening of diffraction lines and the size of the crystal. Nevertheless, it is widely acknowledged that lattice strain plays a substantial role in the broadening of diffraction lines. Table 1 gives the range of obtained lattice strains for the developed ferrites. The Williamson–Hall equation (eq 2), which incorporates the influences of both crystal dimensions and internal strain, is used to calculate the lattice strain.[10]

$$\beta \cos\theta = 4\varepsilon \sin\theta + \frac{0.9\lambda}{t_{WH}} \tag{2}$$

where β is the full-width at half-maximum of the diffraction line, λ is the wavelength of the incident X-ray radiation, K is the shape factor, t_{WH} is the crystallite size, θ is the Bragg angle, and ε is the lattice strain.

It was found that the values of D were in the range of 22−42 nm, and Akther Hossain and Rahman[19] reported values that were comparable to these observations. Tables 1 and 2 summarize the results from XRD analysis. The X-ray density, denoted by the symbol d_{xrd}, was determined for each ferrite sample as follows.[10]

$$d_{xrd} = \frac{8M}{Na^3} \tag{3}$$

where M is the molecular weight of the sample, N is Avogadro's number, 8 is the number of molecules per unit cell, and a^3 is the volume of the unit cell.

The idea of liquid immersion was used in order to calculate each ferrite's bulk density. The medium for the suspension xylene was utilized, and using the Archimedes principle, the values of d_{bulk} were calculated. The percentage porosity (p%) of the developed ferrite samples was calculated using the following equation:[10]

$$p\% = 100\left(1 - \frac{d_{app}}{d_{xrd}}\right) \tag{4}$$

As demonstrated in Table 1, the X-ray density of $Ni_{0.25-x}Co_xCu_{0.20}Zn_{0.55}Fe_2O_4$ at x = 0.00 is 5.47 g/cm^3. However, upon substituting with Co, at x = 0.25, the X-ray density increased to 5.50 g/cm^3. This rise in the X-ray density may be related to the atomic weight and density of substituting Co^{2+} in place of Ni^{2+} ions since the atomic weight of Co^{2+} (i.e., 58.93 amu) is higher than that of Ni^{2+} (58.69 amu). The range

Table 2. Compositional Data on the Lattice Parameter (a), Tetrahedral Site Radius (r_A), Octahedral Site Radius (r_B), Theoretical Lattice Parameter (A_{th}), and Molecular Weight (M_A) of $(Ni_{0.25-x}Co_xCu_{0.20}Zn_{0.55})Fe_2O_4$

content (x)	a (Å)	r_A (Å)	r_B (Å)	A_{th} (Å)	M_A (amu)
0.00	8.34	0.5727	0.7154	8.378	239.03
0.05	8.35	0.5750	0.7178	8.368	239.04
0.10	8.35	0.5754	0.7183	8.349	239.06
0.15	8.37	0.5775	0.7183	8.328	239.07
0.20	8.37	0.5802	0.7235	8.299	239.08
0.25	8.37	0.5802	0.7235	8.267	239.09

Table 1. Properties of the Developed Ferrites Obtained from XRD Analysis

content (x)	crystallite size from XRD (nm)	grain size from SEM (μm)	lattice parameter (Å)	lattice strain (10^{-3})	X-ray density (g/cm^3)	bulk density (g/cm^3)	porosity (%)
0.00	22.8	0.87	8.34	14.3	5.47	3.20	48.10
0.05	38.81	0.88	8.34	17.8	5.45	3.17	36.66
0.10	39.28	0.93	8.35	23.7	5.44	3.47	61.36
0.15	42.24	0.93	8.37	25.6	5.41	2.80	35.63
0.20	32.24	0.81	8.37	21.9	5.40	2.97	53.51
0.25	41.78	0.77	8.37	23.5	5.50	2.90	73.36

https://doi.org/10.1021/acsomega.3c03757
ACS Omega 2023, 8, 30508−30518

of X-ray density was from 5.40 to 5.50 m/cm^3. Because of the entry of Co^{2+} ions into an inverted spinel structure, the bulk density exhibited a modest drop, as seen in Table 1. This in turn gave rise to corresponding enhancement in the porosities. This also may be explained on the basis of stoichiometry, the technique of preparation, and the circumstances of the heat treatment, all of which are dependent on the anomalous densification and crystal defects.

The parameters presented in Table 2 are calculated using following relations:[10]

$$r_A = C_{AZn}r(Zn^{2+}) + C_{ANi}r(Ni^{2+}) + C_{ACo}r(Co^{2+}) + C_{ACu}r(Cu^{2+}) + C_{AFe}r(Fe^{2+}) \quad (5)$$

$$r_B = {}^1/_2[C_{BNi}r(Ni^{2+}) + C_{BCo}r(Co^{2+}) + C_{BCu}r(Cu^{2+}) + C_{BFe}r(Fe^{2+})] \quad (6)$$

where $r(Zn^{2+})$ = 0.74 Å, $r(Co^{2+})$ = 0.72 Å, $r(Fe^{2+})$ = 0.64 Å, $r(Ni^{2+})$ = 0.74 Å, and $r(Cu^{2+})$ = 0.74 Å. C_{AZn}, C_{ACo}, and C_{AFe} are concentrations of corresponding ions at A sites, and C_{BNi}, C_{BCo}, C_{BCu}, and C_{BFe} are concentrations of corresponding ions at B sites.

$$A_{th} = \frac{8}{3\sqrt{3}}[(r_A + R_0) + \sqrt{3}(r_B + R_0)] \quad (7)$$

where r_A and r_B are the radii of the tetrahedral (A) and octahedral (B) sites, respectively, and R_o is the radius of the oxygen anion (1.32 Å).

3.2. Morphological Analysis (SEM). Figure 4 (and Figure S1) depicts the results of FE-SEM analysis of the developed ferrites. All of the ferrite samples exhibit the agglomerations of tiny particles with irregular shapes and size, which are characteristics of the sol−gel autocombustion pathway. The average grain size (d) was calculated by the linear intercept method.[20] The average grain size was observed to be in the range of 0.77−0.93 μm. The grain size (d) did not agree well with those obtained from the crystallite size (D) by XRD analysis, and this is because grain growth and grain movements hinder the formation of crystallites.

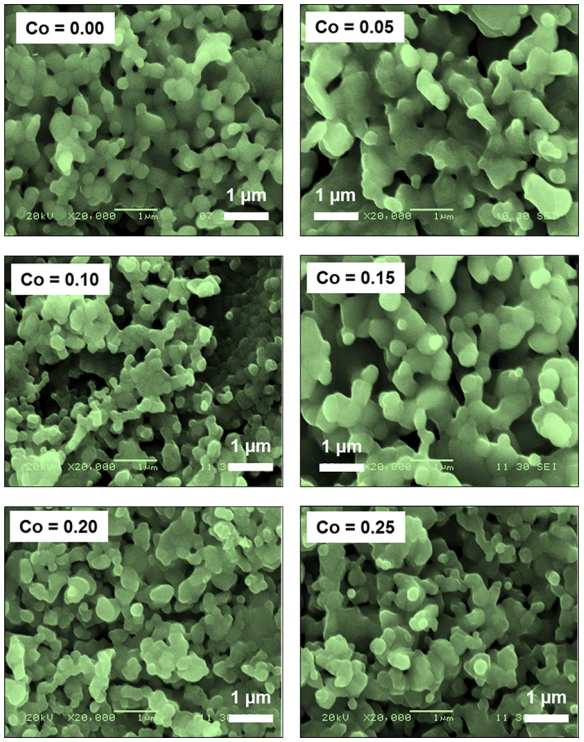

Figure 4. FE-SEM images of all the developed Co-substituted NiCuZn ferrites.

The morphologies seem to be a result of colloidal connections of tiny particles with some empty spaces and voids. However, the addition of higher Co resulted in the enhanced aggregation of the colloidal backbone of the ferrite. During the sol−gel process, mixed ferrite evolved in the form of micrometer-sized secondary aggregation of colloidal particles. This secondary aggregation is microscopic in size. The amount of Co that is present in the sol has an effect on the size of these aggregates. The size of these aggregates has grown as the amount of doping present in the system.

Furthermore, it should not come as a surprise that the inclusion of copper has a significant impact on the microstructure of the generated composite ferrite. Because it segregates to the grain boundaries, copper makes it easier for the liquid phase to become sintered, and it also speeds up the rates at which cations may diffuse between grains.[21] It is reasonable to anticipate that there will be equal distribution of grain size if the force that drives grain boundary movement on each grain is the same throughout. On the other hand, an aberrant grain development will occur in the event that the pushing force is not homogeneous.[22] The nonhomogeneous driving force that liquid-phase sintering exerts on the grains may be credited with contributing to the nonuniformity in grain size that was observed in this particular instance.[18,23] The sample with a Co value of 0.15 was found to have the largest particles, measuring 0.93 μm in size.

3.3. Elemental Analysis (EDAX). Energy-dispersive X-ray spectroscopy (EDAX or EDS) was used for chemical characterization and elemental analysis of ferrite samples. Figure 5 depicts the EDAX spectrographs of $Ni_{0.25-x}Co_xCu_{0.20}Zn_{0.55}Fe_2O_4$ with x = 0−0.25 ferrites. EDAX peaks belonging to the elements Ni, Cu, Zn, Co, Fe, and O were found, confirming the existence of corresponding ions according to the original stoichiometry being investigated. In Table 3, the compositional atomic percentages of Ni^{2+}, Cu^{2+}, Zn^{2+}, Co^{2+}, Fe^{3+}, and O^{2-} ions in ferrite samples as determined by EDAX are listed.

3.4. Electrical Properties. *3.4.1. DC Electrical Resistivity.* Figure 6 shows the response of DC electrical resistivity of ferrites as a function of temperature. The nature explains the drop in the ferrite resistance with increasing temperature. This nature validates the semiconductor type of the developed ferrites. Table 4 provides tabular data for DC resistivity, AC resistivity, Curie temperature, dielectric constant, complex dielectric constant, dielectric loss factor, and activation energy. The activation energy and the underlying conduction mechanism were both significantly affected by the incorporation of cobalt. From this, we might infer that polaron hopping is responsible for the conduction seen in ferrites.[24] When describing the conduction mechanism in ferrites, the Verwey concept might be useful. Different regions of temperature are said to be generated as a consequence of the conduction and hopping of extrinsic-type carriers and polarons. Two sections separated by the Curie point indicated that ferrimagnetic ordering affected the conductivity process by having different slopes. Conduction in ferrites is mostly the

https://doi.org/10.1021/acsomega.3c03757
ACS Omega 2023, 8, 30508−30518

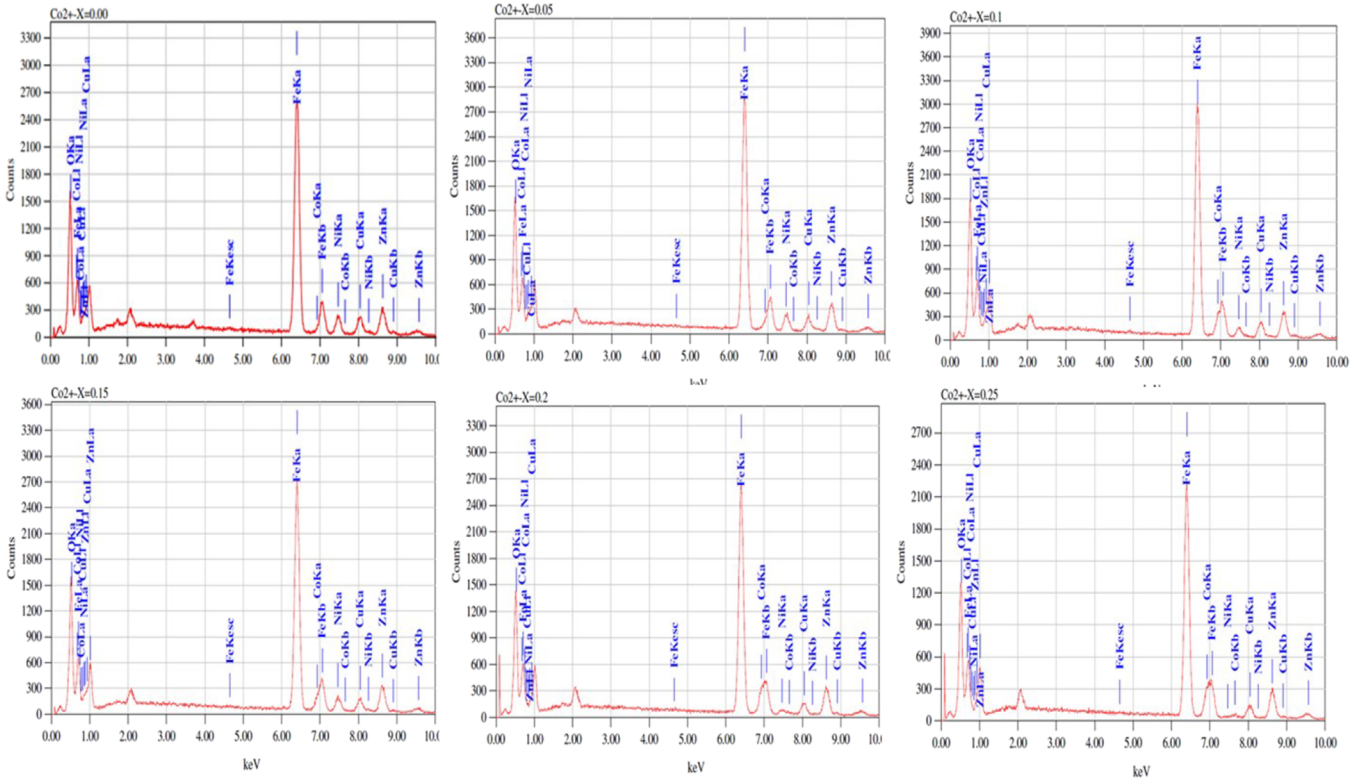

Figure 5. EDAX spectra of all the developed Co-substituted NiCuZn ferrites.

Table 3. Compositional Data on the Atomic Percentage of Elements in $Ni_{0.25-x}Co_xCu_{0.20}Zn_{0.55}Fe_2O_4$ EDAX Analysis

	atomic percentage of as-prepared ferrites					
content (x)	Ni^{2+} (%)	Cu^{2+} (%)	Zn^{2+} (%)	Fe^{3+} (%)	O^{2+} (%)	Co^{2+} (%)
0.00	6.42	7.78	13.48	52.28	20.04	0.00
0.05	5.86	6.20	15.41	52.26	19.46	0.81
0.10	5.11	5.79	14.93	51.95	19.73	2.48
0.15	3.56	6.69	13.69	52.34	19.70	4.02
0.20	1.83	5.38	15.42	53	18.69	5.68
0.25	0.45	5.45	15.35	52.36	20.06	6.33

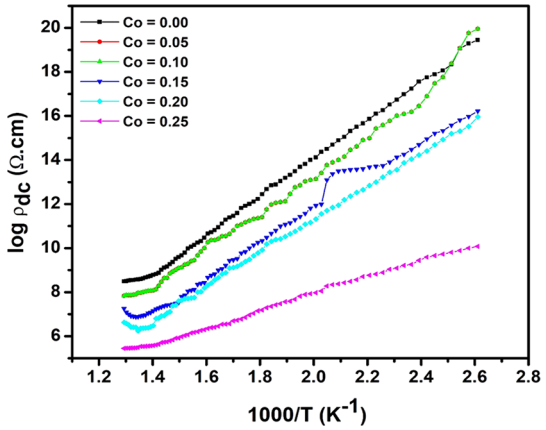

Figure 6. DC resistivity as a function of temperature for all the developed ferrites.

result of electron hopping at the B site; therefore, the decrease in DC resistivity due to Co substitution may be explained by a reduction in this hopping.[25,26]

Table 4. Compositional Data of DC Resistivity, AC Resistivity, Curie Temperature, Dielectric Constant, Complex Dielectric Constant, Dielectric Loss Factor, and Activation Energy of the Developed Ferrites $Ni_{0.25-x}Co_xCu_{0.20}Zn_{0.55}Fe_2O_4$

content (x)	DC resistivity (Ω cm)	AC resistivity (Ω cm)	activation energy (eV)	Curie temperature from DC resistivity (°C)
0.00	2.8×10^5	6.4×10^{10}	0.73	250
0.05	7.5×10^3	1.83×10^8	1.11	235
0.10	4.8×10^3	6.7×10^7	1.20	200
0.15	4.3×10^3	9.0×10^7	0.94	190
0.20	2.5×10^3	3.2×10^6	0.69	170
0.25	1.4×10^3	2.7×10^6	0.61	160

The DC resistivity of a sintered ferrite is the most important characteristic for MLCI applications. This is because the resistivity has a major effect on the electroplating procedure for electronic components. When Co^{2+} is present, the resistivity of the material drops, as shown in Table 4. It is believed that electrons in ferrites conduct by moving from the more electronegative Fe^{2+} to the more positive Fe^{3+} as they go through the material. In Co^{2+}-substituted NiCuZn ferrites, it was discovered that the B sites were being occupied by the ions Ni^{2+}, Fe^{+}, and Cu^{2+}. The conductivity will automatically increase when there is a larger concentration of Fe^{2+}, and as a consequence, the resistance will decrease. As a result of this, the decrease in DC resistivity that was seen to coincide with an increase in the Co^{2+} content may be ascribed to the presence of more Fe^{+} ions. This is because an increase in the Co^{2+} content was observed to occur simultaneously with the decrease in DC resistivity. During the process of sintering, there may be an equilibrium that looks like

https://doi.org/10.1021/acsomega.3c03757
ACS Omega 2023, 8, 30508−30518

$$Fe^{3+} + Co^{2+} = Fe^{2+} + Co^{3+}$$

With an increase in the Co^{2+} content comes an increase in the amount of Fe^{2+} that is generated, which leads to an enhanced possibility of electron hopping and a decreased resistance.

Furthermore, as ferrites form closed packed oxygen lattices with the cations over the tetrahedral (A) and octahedral (B) sites, the separation between two metal ions residing on octahedral sites is smaller than the separation between a metal ion on an octahedral site and an ion on the tetrahedral site. Hence, the probability of electron hopping between octahedral and tetrahedral sites is very small as compared to the ions occurring on octahedral sites only. The electron hopping among the ions of tetrahedral sites is not possible as there are only Fe^{3+} ions. The Fe^{2+} ions reside only at octahedral sites. The hopping mechanism depends on the distance between metal ions and the mobility of charge carriers. The presence of Co^{2+} ions on the octahedral sites increases the distance between metal ions of the octahedral sites and enhances the electron transfer between iron ions. Hence, the conduction mechanism in Co^{2+}-substituted NiCuZn inverse spinels can be explained using the hopping mechanism. The conduction mechanism of ferrite exhibits slight variations compared to that of semiconductors. The temperature dependence of mobility in ferrites affects conductivity, while the concentration of charge carriers remains relatively constant with increasing temperature ($n \approx 10^{22}$ cm^{-3}).[13] Furthermore, the charge carriers exhibit a high concentration in proximity to the magnetic ions. The primary mode of conduction is thus attributed to the transfer of 3d electrons (at metal ions) from Fe^{3+} to Fe^{2+}.[13]

3.4.2. AC Electrical Resistivity. For MLCI application, AC resistivity is an essential parameter of NiCuZn ferrite. At room temperature, as a function of frequency, the AC resistivity of the developed ferrites is determined (see Figure 7). The

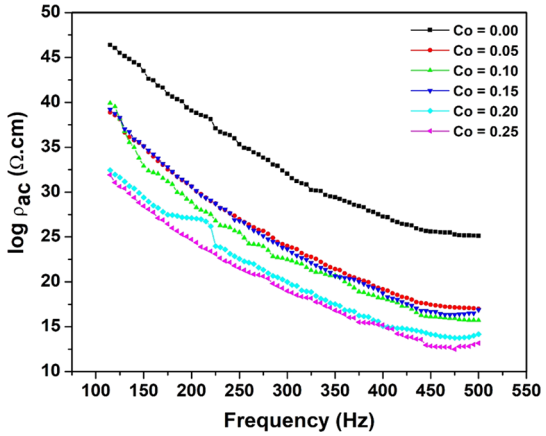

Figure 7. AC resistivity as a function of temperature for all the developed ferrites.

electrical resistivity showed a tendency toward the lower side as the frequency increased. As the applied frequency increases, there is an increased probability of jumping of an electron through $Fe^{3+} \leftrightarrow Fe^{2+}$ ions. The increased concentration of Fe^{2+} ions induces electron hopping $Fe^{3+} \leftrightarrow Fe^{2+}$ at B sites thereby reducing resistivity.

3.4.3. Dielectric Constant as a Function of Frequency (ε′). Figure 8 displays the dielectric constant of the ferrites, denoted

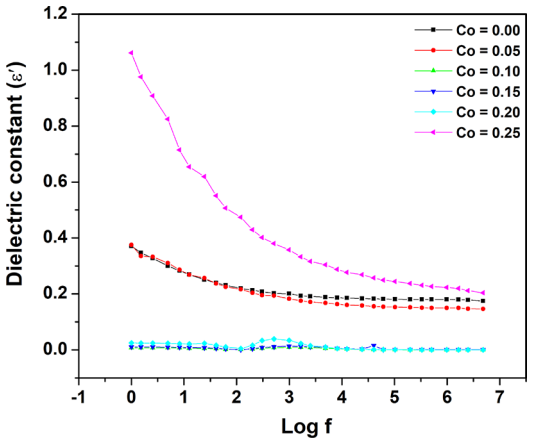

Figure 8. Dielectric constant (ε') of the ferrites as a function of frequency.

by ε' as a function of frequency at room temperature. The dielectric constant of all of the ferrites decreased very quickly when the frequency was raised, and as the frequency was increased even more, they eventually achieved a value that was constant. The fact that the dielectric test showed this trend[27] is evidence that the material has ferromagnetic activity. In addition, the conduction mechanism in ferrites, which is the location where electron hopping takes place, is the primary factor that decides the dielectric properties of the material.

Furthermore, the phenomenological hypothesis proposed by Koop provides an explanation for the mechanism of conductivity found in dielectric systems. It has been found that when an electric current travels through the interfaces of two distinct electric media, for as much of their distinctness as the different electric media possess the conductivities, surface charges accumulate at the interfaces, which results in the interfacial polarization of the boundaries. At lower frequencies, these space charges align themselves with the electric field that is being applied; however, as the frequency increases, the dipoles are unable to harmonize with the frequency of the applied field; consequently, their contribution is small, and the dielectric constant continues to decrease. The grains that make up the samples are completely conductive, and they are separated by grain boundaries that are insulating. According to the postulates of Koop's phenomenological theory, for the grain when it comes to low frequencies, boundaries are effective, whereas grains shine when it comes to high frequencies. As a result, low polarization at higher frequencies causes a reduction in the dielectric constant.

3.4.4. Complex Dielectric Constant as a Function of Frequency (ε″). In addition to the dielectric constant, the complex dielectric constant, which is represented by the symbol ε'', was investigated and analyzed as a function of frequency, as is illustrated in Figure 9.

When the frequency was increased, it exhibited a decrease in the value of ε'', and after a certain frequency, it responded independently against the frequency, particularly on the higher frequency side. The presence of Maxwell–Wagner interfacial polarization,[21,22] which is found in inhomogeneous dielectrics, can provide an explanation for this phenomenon. Large values of dielectric constants were reported at low frequencies as a result of the prevalence of Fe^{2+} ions, interfacial dislocations, oxygen vacancies, and grain boundary defects.[28] Table 5 gives a comparative chart of the dielectric constant, complex dielectric

https://doi.org/10.1021/acsomega.3c03757
ACS Omega 2023, 8, 30508−30518

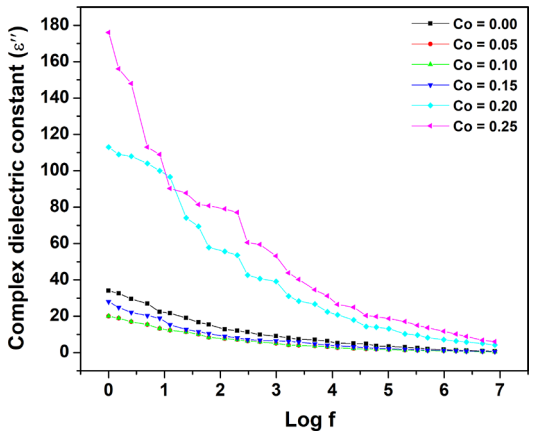

Figure 9. Complex dielectric constant (ε'') of the ferrites as a function of frequency.

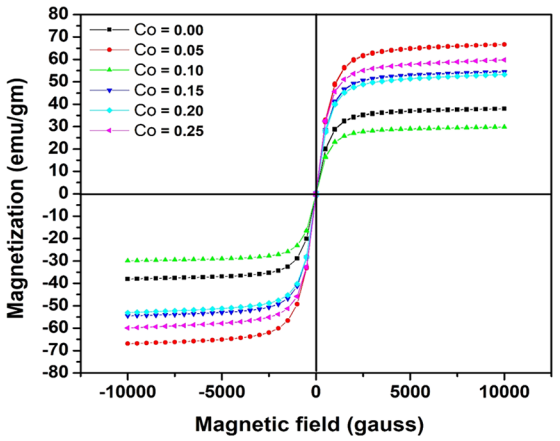

Figure 10. Magnetic hysteresis loops of Co^{2+}-substituted NiCuZn ferrites.

constant, and dielectric loss factor of the developed ferrites $Ni_{0.25-x}Co_xCu_{0.20}Zn_{0.55}Fe_2O_4$.

Table 5. Compositional Data of the Dielectric Constant, Complex Dielectric Constant, and Dielectric Loss Factor of the Developed Ferrites $Ni_{0.25-x}Co_xCu_{0.20}Zn_{0.55}Fe_2O_4$

content (x)	dielectric constant (ε')	complex dielectric constant (ε'')	dielectric loss factor (tan δ)
0.00	37.10	34.0	0.02391
0.05	15.58	20.2	0.02641
0.10	12.00	20.3	0.03352
0.15	15.00	28.3	0.02619
0.20	25.72	11.3	0.03115
0.25	25.74	20.4	0.03803

3.5. Magnetic Properties. *3.5.1. Magnetization (VSM).* The VSM analysis was carried out in order to investigate the magnetic properties such as M_s, H_c, and M_r/M_s of the developed ferrites. The magnetic properties of spinel ferrites are influenced by a number of different parameters, such as the synthesis technique, the distribution of cations on tetrahedral and octahedral sites, and the crystallite size.[29] It is possible to alter the magnetic properties of ferrite nanoparticles by utilizing a distinct combination of doping ions, altering the synthesis method, or adjusting the calcination temperature.[30,31] Figure 10 depicts the typical hysteresis loops of as-prepared ferrites measured at room temperature. All of the samples displayed the same general shape for their magnetic hysteresis, which is evidence that the material may be magnetically ordered. Table 6 displays the results of calculations made using the hysteresis loop to determine the values of magnetic properties such as saturation magnetization (M_s), coercivity, and remanence for each ferrite composition. It is observed that the hysteresis loops of ferrite samples are thin and narrow, which indicated that the ferrites are magnetically soft with low coercivity and possess ferrimagnetic nature. It is observed that saturation magnetization (M_s) is found to be in the range of 10.40−21.0 emu/g. Maximum M_s = 21.50 emu/g is found for the sample with x = 0.05. However, a definite trend of variation of M_s could not be defined. The magnetic moment of Ni^{2+} (2.3 μB) and of Co^{2+} (3.87 μB) plays a key role in the magnetic properties during the substitution process,[32] but Co^{2+} showed partial distribution between A sites and B sites, while Zn^{2+} has strong occupancy on A sites. According to Néel's two-sublattice model, A−B exchange interaction becomes strong due to replacement of Ni^{2+} ions by Co^{2+} ions at the respective sites, and the Bohr magneton (n_B) increases with the increase of Co^{2+} ions.

In addition, Table 6 gives the probable cation distribution and experimental magnetic moments for various compositions of ferrites $Ni_{0.25-x}Co_xCu_{0.20}Zn_{0.55}Fe_2O_4$ with x = 0−0.25. The highest experimental magnetic moment of 2.56 was obtained for Co = 0.25. Meanwhile, the high α_{y-k} value of 45°01′19″ was obtained for pristine NiCuZn. The drop in α_{y-k} is mostly attributable to the substitution of Co, which possesses no magnetic moment.

Additionally, the theoretical magnetic moment is calculated and compared with the experimental value. According to Néel's two-sublattice model of ferrimagnetism, the theoretical value of the magnetic moment per formula unit can be expressed as[10]

$$|\mu_{th}| = |\mu_B| - |\mu_A| \tag{8}$$

where μ_B and μ_A are the magnetic moments of the cations at the B and A sites at a particular dopant concentration (x). Using the obtained cation distribution, μ_B and μ_A can be calculated by the following equation:

$$\mu_B \text{ or } \mu_A = \sum_{i=1}^{N} C_i \times \mu_i \tag{9}$$

where N is the number of cations in B sites (or A sites), C_i is the concentration of cations, and μ_i is the magnetic moment of cations "i", amounting to 2, 3, 0, 3, and 5 μ_B for Ni^{2+}, Cu^{2+}, Zn^{2+}, Co^{2+}, and Fe^{3+}, respectively.

3.5.2. AC Susceptibility (χ_T/χ_{RT}). The normalized AC susceptibility of the ferrites as a function of temperature is depicted in Figure 11. This parameter is represented by the symbol (χ_T/χ_{RT}). From the graph, it is clearly seen that the values of χ_T/χ_{RT} in all ferrites dropped dramatically as they drew closer to the Curie temperature. Due to enough thermal energy to disrupt the aligned moments of spins, the drop in the susceptibility values is seen. This behavior in general takes place when the temperature exceeds the Curie temperature. In this context, it refers to the material's transition from a ferrimagnetic state to a paramagnetic state.

3.5.3. Initial Permeability and Its Real and Imaginary Parts (μ_i, μ', and μ''). The magnetic permeability of any magnetic material can be thought of as a measure of how well

https://doi.org/10.1021/acsomega.3c03757
ACS Omega 2023, 8, 30508−30518

Table 6. Cation Distribution, Magnetic Moment, M_s, M_r/M_s, and Yafet−Kittel Angle of the Developed Ferrites $Ni_{0.25-x}Co_xCu_{0.20}Zn_{0.55}Fe_2O_4$

content (x)	cation distribution	μ_B	μ_{th}	α_{y-k}	M_s (emu/g)	M_r/M_s
0.00	$(Zn_{0.55}Ni_{0.10}Fe_{0.35})$ $[Ni_{0.15}Cu_{0.20}Fe_{1.65}]O_4$	1.62	3.70	45°01′19″	20.78	0.00581
0.05	$(Zn_{0.55}Ni_{0.08}Co_{0.02}Fe_{0.35})$ $[Ni_{0.12}Co_{0.03}Cu_{0.20}Fe_{1.65}]O_4$	2.11	4.28	43°03′36″	21.50	0.01896
0.10	$(Zn_{0.55}Ni_{0.06}Co_{0.04}Fe_{0.35})$ $[Ni_{0.09}Co_{0.06}Cu_{0.20}Fe_{1.65}]O_4$	1.70	3.61	41°24′35″	10.40	0.01867
0.15	$(Zn_{0.55}Ni_{0.04}Co_{0.06}Fe_{0.35})$ $[Ni_{0.06}Co_{0.09}Cu_{0.20}Fe_{1.65}]O_4$	2.33	4.57	37°21′04″	15.32	0.03343
0.20	$(Zn_{0.55}Ni_{0.02}Co_{0.08}Fe_{0.35})$ $[Ni_{0.03}Co_{0.12}Cu_{0.20}Fe_{1.65}]O_4$	2.27	4.36	38°23′05″	16.07	0.05433
0.25	$(Zn_{0.55}Co_{0.10}Fe_{0.35})$ $[Ni_{0.03}Co_{0.12}Cu_{0.20}Fe_{1.65}]O_4$	2.56	4.63	35°11′23″	17.44	0.04368

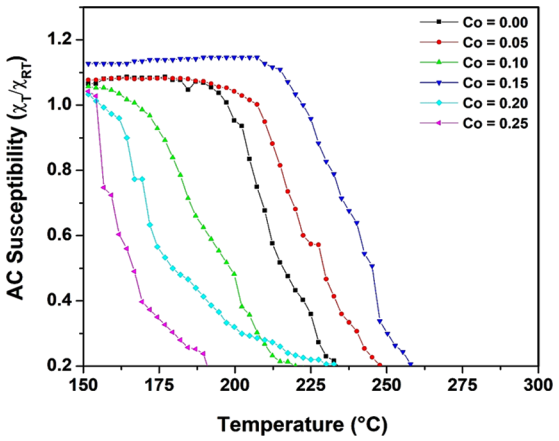

Figure 11. Normalized AC susceptibility (χ_T/χ_{RT}) of the ferrites as a function of temperature.

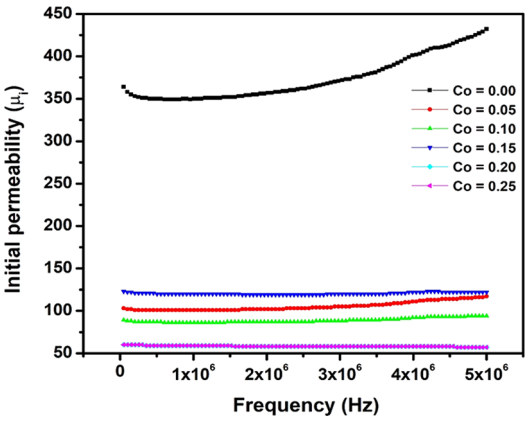

Figure 12. Initial permeability as a function of frequency of the ferrites.

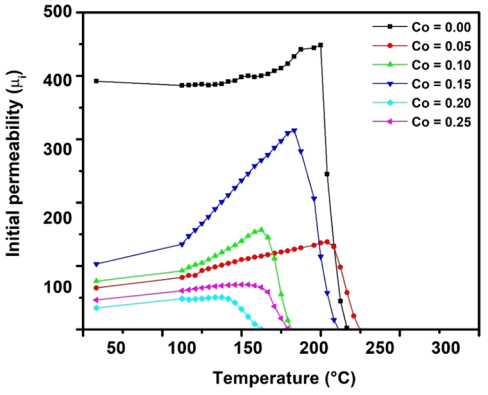

Figure 13. Initial permeability as a function of temperature.

that material works. Frequency dispersion and temperature dispersion can both be used to describe the initial permeability (μ_i) of a ferrite material.[33] μ' gives the stored energy, which is the component of magnetic induction (M) in phase with the alternating magnetic field H. This is called the real part of initial permeability. μ'' gives the dissipative energy or energy loss, which is 90° out of phase with the applied magnetic field H. This is called the imaginary part of initial permeability.

At room temperature, the initial permeability (μ_i) of developed ferrites was measured between 100 kHz and 5 MHz. The μ_i value of the ferrites (except $x = 0$) exhibited a behavior that was constant over the entire frequency range under study. However, from the graph, it is clearly seen that the cobalt-substituted NiCuZn ferrites show low initial permeability values, as compared to native NiCuZn ferrites (Figure 12).

Along with the function of frequency, the initial permeability was also studied as a function of temperature (see Figure 13). In this case, the μ_i value of the ferrites exhibited a behavior that has a gradual increase up to a particular temperature, and beyond that, it fell down steeply, with a further increase in temperature. In the case of Co substitution, the value of μ_i is the highest at $x = 0.15$. For the rest of the ferrite samples (except $x = 0.00$), the initial permeability was almost similar. The lowest μ_i was observed for ferrite with $x = 0.20$.

This decrement in the permeability values is caused by the substitution of cobalt for nickel, which results in an increase in the magnetostriction constant. In addition to that, the rotational permeability (μ_{rk}) and wall permeability (μ_w) were computed utilizing the following formulae:

$$\mu_{rk} = 1 + 2\pi M^2 s/lk_1 l \quad (10)$$

$$\mu_w = \mu_i - (\mu_{rk} - 1) \quad (11)$$

During hysteresis behavior, magnetocrystalline anisotropy is a key factor. Figure 14 shows how the real part of the initial permeability (μ') changes as the frequency changes. The steady state was shown by the constant value of the real part of the initial permeability. The real part of initial permeability (μ') was the highest for Co = 0.15. Again, the reason for lower (μ') values than native NiCuZn is because cobalt was used instead of nickel.

Figure 15 presents a plot of the imaginary component of the initial permeability, denoted by μ'', against the frequency. The frequency dispersion can be observed in the imaginary component of the initial permeability (μ''). In the low frequency area, there is a quick drop in the μ'' values, but otherwise, they almost remain more or less the same at the higher frequency side.

It is interesting to note that despite the fact that Co^{2+} ions have a ferrimagnetic characteristic, there is a discernible decrease in μ_i, μ', and μ'' with an increase in the number of dopant ions (i.e., cobalt). This suggests that the source of the

https://doi.org/10.1021/acsomega.3c03757
ACS Omega 2023, 8, 30508−30518

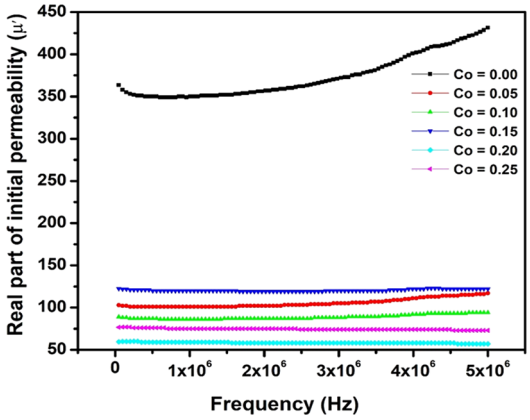

Figure 14. Real part of initial permeability (μ') of the developed ferrites as a function of frequency.

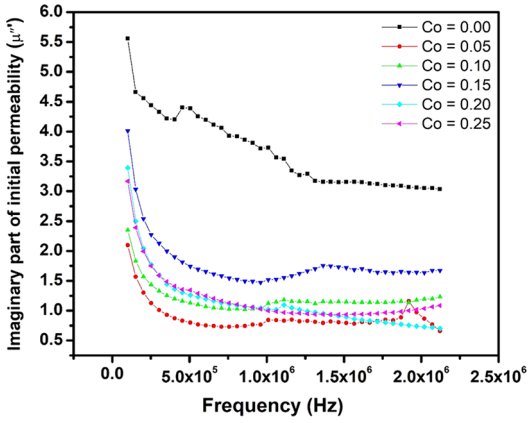

Figure 15. Imaginary part of the initial permeability (μ'') of the developed ferrites as a function of frequency.

variation in permeability observed in the present ferrite samples is due to changes in microstructure, specifically lattice distortion and spin frustration. A smaller grain size has been observed, which has led to a considerable reduction in the amount of domain wall movement. The observations of magnetic properties of ferrites can be explained by the modification of average sizes of crystallites, which is dependent on the degree of defectiveness of the crystal lattice, particle size and shape, morphology of structure in homogeneous particles, and the interactions of particles with the surrounding matrix and neighboring particles. In other words, the magnetic properties of ferrites are caused by the modification of the average sizes of crystallites.

Table 7 gives an account of the complete picture of magnetic properties of the developed ferrites.

4. CONCLUSIONS

In conclusion, we have adopted citrate gel autocombustion to develop spinel-type Co^{2+}-substituted NiCuZn ferrites, with the general system $Ni_{0.25-x}Co_xCu_{0.20}Zn_{0.55}Fe_2O_4$ at x = 0.00−0.25 and a step size of 0.05. Using citrate as a chelating agent, a single-phase ferrite material with a high density and dense microstructure was constructed. As evident from FE-SEM, adding cobalt causes ferrite's colloidal backbone to aggregate. According to the original stoichiometry of Co-substituted NiCuZn ferrite, the EDAX peaks of Ni, Cu, Zn, Co, Fe, and O proved the existence of matching ions. Speaking about electrical properties, NiCuZn ferrites' electrical resistivity (AC and DC both) decreases with Co^{2+} substitution in the parent ferrite. When the frequency was raised, all ferrites' dielectric characteristics (ε' and ε'') immediately fell and stabilized with a further increase in the frequency. Co^{2+} substitution in NiCuZn lowers the ferrites' magnetic characteristics, according to magnetic property analysis. The VSM investigation found that all ferrite samples had a regular magnetic hysteresis. This form indicates a magnetically organized material. The saturation magnetization in the ferrite was the highest when x = 0.05. When the ferrite system had more cobalt (x = 0.20), the Curie temperature dropped. The ferrites' μ_i value increased gradually up to a certain temperature and then dropped steeply as the temperature increased. The steady state was indicated by the constant real component of the initial permeability, μ'. At low frequencies, the μ'' values decline quickly, whereas at higher frequencies, they stay the same. Based on the conducted investigations and obtained results, Co^{2+}-substituted NiCuZn ferrites may be suitable for microwave absorption applications with enhanced electromagnetic properties.

■ ASSOCIATED CONTENT

Supporting Information

The Supporting Information is available free of charge at https://pubs.acs.org/doi/10.1021/acsomega.3c03757.

Table of data comparison and FE-SEM images of all the developed Co-substituted NiCuZn ferrite samples (PDF)

Table 7. Compositional Data of Developed Ferrites

content (x)	0.00	0.05	0.10	0.15	0.20	0.25
crystallite size-XRD (nm)	22.8	38.81	39.28	42.24	32.24	41.78
saturation magnetization M_s (emu/g)	20.78	21.50	10.40	15.32	16.07	17.44
coercivity, H_c (Gauss)	2.99	5.86	8.32	8.96	15.14	11.48
anisotropy constant ($k_1 \times 10^4$) (erg/cc)	4.03	3.4	3.25	3.11	2.96	2.85
Yafet−Kittel angle (α_{y-k})	45°1′19″	43°3′6″	41°24′35″	37°21′4″	38°23′5″	35°11′23″
initial permeability (μ_i)	429	117	94	122	57	73
real part of μ_i (μ')	431	116	93	12	56	72
Curie temperature from AC susceptibility	230 °C	248 °C	220 °C	255 °C	231 °C	190 °C
imaginary part of μ_i (μ'')	14.71	0.17	0.44	0.59	0.62	0.76
Curie temperature from μ_i (°C)	225	230	180	223	130	180
wall permeability (μ_w)	135	240	161	78	107	117
rotational permeability (μ_r)	102	110	25	55	61	72

https://doi.org/10.1021/acsomega.3c03757
ACS Omega 2023, 8, 30508−30518

AUTHOR INFORMATION

Corresponding Authors

Digambar Nadargi − *School of Physical Sciences, Punyashlok Ahilyadevi Holkar Solapur University, Solapur 413255, India; Centre for Materials for Electronics Technology, CMET, Thrissur 680581, India;* orcid.org/0000-0003-2092-2590; Email: digambar_nadargi@yahoo.co.in

Sharad S. Suryavanshi − *School of Physical Sciences, Punyashlok Ahilyadevi Holkar Solapur University, Solapur 413255, India;* orcid.org/0000-0002-3996-1998; Email: sssuryavanshi@rediffmail.com

Authors

Babasaheb Ingale − *Department of Physics and Electronics, Azad Mahavidyalaya, Dist. Latur 413520, India*

Jyoti Nadargi − *Department of Physics, Santosh Bhimrao Patil College, Solapur 413221, India*

Rangrao Suryawanshi − *Department of Physics and Electronics, Azad Mahavidyalaya, Dist. Latur 413520, India*

Hamid Shaikh − *SABIC Polymer Research Centre, Department of Chemical Engineering, King Saud University, Riyadh 11421, Saudi Arabia*

Mohammad Asif Alam − *Center of Excellence for Research in Engineering Materials (CEREM), King Saud University, Riyadh 11421, Saudi Arabia*

Mohaseen S. Tamboli − *Korea Institute of Energy Technology (KENTECH), Naju, Jeollanam-do 58330, Republic of Korea*

Complete contact information is available at: https://pubs.acs.org/10.1021/acsomega.3c03757

Notes

The authors declare no competing financial interest.

ACKNOWLEDGMENTS

The authors extend their appreciation to the Deputyship for Research and Innovation, "Ministry of Education" in Saudi Arabia for funding this research (IFKSUOR3-108-1).

REFERENCES

(1) Rabbani, A.; Haghniaz, R.; Khan, T.; Khan, R.; Khalid, A.; Naz, S. S.; Ul-Islam, M.; Vajhadin, F.; Wahid, F. Development of bactericidal spinel ferrite nanoparticles with effective biocompatibility for potential wound healing applications. *RSC Adv.* **2021**, *11*, 1773−1782.

(2) Almessiere, M. A.; Slimani, Y.; Güngüneş, H.; Korkmaz, A. D.; Zubar, T.; Trukhanov, S.; Trukhanov, A.; Manikandan, A.; Alahmari, F.; Baykal, A. Influence of Dy^{3+} Ions on the Microstructures and Magnetic, Electrical, and Microwave Properties of $[Ni_{0.4}Cu_{0.2}Zn_{0.4}]$-$(Fe_{2-x}Dy_x)O_4$ ($0.00 \leq x \leq 0.04$) Spinel Ferrites. *ACS Omega* **2021**, *6*, 10266.

(3) Kabbur, S. M.; Nadargi, D. Y.; Kambale, R. C.; Ghodake, U. R.; Suryavanshi, S. S. Microstructure and magnetic interactions of Co^{2+} substituted NiCuZn ferrites. *J. Magn. Magn. Mater.* **2021**, *517*, No. 167376.

(4) Ge, X.; Li, H.; Zheng, H.; Zheng, P.; Zheng, L.; Zhang, Y. Electromagnetic Performance of NiMgCuZn Ferrite for Hyperthermia Application in Cancer Treatment. *ACS Omega* **2023**, *8*, 16647.

(5) Aphesteguy, J.; Damiani, A.; DiGiovanni, D.; Jacobo, S. Microwave-Absorbing Characteristics of Epoxy Resin Composites Containing Nanoparticles of NiZn- and NiCuZn-Ferrites. *Phys. B* **2009**, *404*, 2713.

(6) Lima, U. R.; Nasar, M. C.; Nasar, R. S.; Rezende, M. C.; Araújo, J. H.; Oliveira, J. F. Synthesis of NiCuZn ferrite nanoparticles and microwave absorption characterization. *Mater. Sci. Eng., B* **2008**, *151*, 238.

(7) Mazen, S. A.; Nawara, A. S.; Abu-Elsaad, N. I. Investigation of dielectric behavior in Ni0.7-xZn0.3MxFe2O4 (M=Mn/Co/Cu) ferrites by impedance spectroscopy. *Ceram. Int.* **2021**, *47*, 9856.

(8) Xiang, R. J.; Shen, X.; Meng, X. Preparation of Co-substituted MnZn ferrite fibers and their magnetic properties. *Mater. Chem. Phys.* **2009**, *114*, 362.

(9) Aziz, C.; Azhdar, B. Synthesis of dysprosium doped cobalt ferrites nanoparticles by solgel auto-combustion method and influence of grinding techniques on structural, Morphological, and magnetic properties. *J. Magn. Magn. Mater.* **2022**, *542*, No. 168577.

(10) Abu-Elsaad, N. I.; Nawara, A. S.; Mazen, S. A. Synthesis, structural characterization, and magnetic properties of Ni−Zn nanoferrites substituted with different metal ions (Mn^{2+}, Co^{2+}, and Cu^{2+}). *J. Phys. Chem. Solids* **2020**, *146*, No. 109620.

(11) Kabbur, S. M.; Waghmare, S. D.; Nadargi, D. Y.; Sartale, S. D.; Kambale, R. C.; Ghodake, U. R.; Suryavanshi, S. S. Magnetic interactions and electrical properties of Tb3+ substituted NiCuZn ferrites. *J. Magn. Magn. Mater.* **2019**, *473*, 99.

(12) Varalaxmi, N.; Sivakumar, K. V. Structural and dielectric studies of magnesium substituted NiCuZn ferrites for microinductor applications. *Mater. Sci. Eng., B* **2014**, *184*, 88.

(13) Abu-Elsaad, N. I.; Mazen, S. A.; Nawara, A. S. Tertiary $Ni_{0.7-x}Zn_{0.3}M_xFe_2O_4$ (M=Mn, Co, and Cu) spinel ferrites: Electrical and dielectric properties. *J. Alloys Compd.* **2021**, *856*, No. 157794.

(14) Hsiang, H.-I.; Wu, J.-L. Copper-rich phase segregation effects on the magnetic properties and DC-bias-superposition characteristic of NiCuZn ferrites. *J. Magn. Magn. Mater.* **2015**, *374*, 367.

(15) Ghasemi, A.; Ghasemi, E.; Paimozd, E. Influence of copper cations on the magnetic properties of NiCuZn ferrite nanoparticles. *J. Magn. Magn. Mater.* **2011**, *323*, 1541.

(16) Rezlescu, E.; Rezlescu, N.; Pasnicu, C.; Craus, M. L. Densinfication by nonmagnetic additives of high frequency lithium-zinc and nickel-zinc ferrites. *J. Magn. Magn. Mater.* **1996**, *157-158*, 487.

(17) Lucas, A.; Lebourgeois, R.; Mazaleyrat, F.; Laboure, E. Temperature dependence of core loss in cobalt substituted NiCuZn ferrites. *J. Magn. Magn. Mater.* **2011**, *323*, 735.

(18) Li, N. H.; Lo, S. L.; Hu, C. Y.; Hsieh, C. H.; Chen, C. L. Stabilization and phase transformation of CuFe2O4 sintered from simulated copper-laden sludge. *J. Hazard. Mater.* **2011**, *190*, 597.

(19) Akther Hossain, A. K. M.; Rahman, M. L. *J. Magn. Magn. Mater.* **2011**, *323*, 1954−1962.

(20) Naidu, K. C. B.; Madhuri, W. *J. Magn. Magn. Mater.* **2016**, *420*, 109−116.

(21) Low, K. O.; Sale, F. R. Electromagnetic Properties of Gel-Derived NiCuZn Ferrites. *J. Magn. Magn. Mater.* **2002**, *246*, 30−35.

(22) Bellad, S. S.; Watawe, S. C.; Chougule, B. K. Microstructure and permeability studies of mixed Li-Cd ferrites. *J. Magn. Magn. Mater.* **1999**, *195*, 57−64.

(23) Su, H.; Tang, X.; Zhang, H.; Zhong, Z.; Shen, J. Sintering dense NiZn ferrite by two-step sintering process. *J. Appl. Phys.* **2011**, *109*, No. 07A501.

(24) Reddy, P. V.; Rao, T. S.; Rao, S. M. D. Electrical conductivity of lithium-nickel ferrites. *J. Less-Common Met.* **1981**, *79*, 191−198.

(25) *CRC Handbook of Chemistry and Physics*; Weast, R. C., Ed.; CRC Press: Boca Raton, 53rd edn, 1972, p. D-120.

(26) Zayat, M.; Levy, D. Blue CoAl2O4 Particles prepared by the sol-gel and citrate-gel methods. *Chem. Mater.* **2000**, *12*, 2763−2769.

(27) Koops, C. G. On the dispersion of resistivity and dielectric constant of some semiconductors at audio frequencies. *Phys. Rev.* **1951**, *83*, 121−124.

(28) Ahmed, M. A.; Bishay, S. T. The magnetic and electrical properties of Cr3 + substituted nickel ferrite. *J. Magn. Magn. Mater.* **2004**, *279*, 178.

(29) Almessiere, M. A.; Slimani, Y.; Güngüneş, H.; Demir Korkmaz, A.; Trukhanov, S. V.; Guner, S.; Alahmari, F.; Trukhanov, A. V.; Baykal, A. Correlation between chemical composition, electrical,

magnetic and microwave properties in Dy-substituted Ni-Cu-Zn ferrites. *Mater. Sci. Eng., B* **2021**, *270*, No. 115202.
(30) Sujatha, C.; Reddy, K. V.; Babu, K. S.; Reddy, A. R.; Rao, K. H. Effects of heat treatment conditions on the structural and magnetic properties of MgCuZn nano ferrite. *Ceram. Int.* **2012**, *38*, 5813−5820.
(31) Kaur, T.; Kaur, B.; Bhat, B. H.; Kumar, S.; Srivastava, A. K. Effect of calcination temperature on microstructure, dielectric, magnetic and optical properties of Ba0. 7La0.3Fe11.7Co0.3O19 hexaferrites. *Phys. B* **2015**, *456*, 206−212.
(32) J., Smit, *Magnetic Properties of Materials*; McGraw-Hill Book Co.: New York, 1971; pp. 216.
(33) Miller, A. Distribution of cations in spinels. *J. Appl. Phys.* **1959**, *30*, 524−S25.

https://doi.org/10.1021/acsomega.3c03757
ACS Omega 2023, 8, 30508−30518